Arch. Min. Sci. **71** (2026), 2, 337-360

Electronic version (in color) of this paper is available: http://mining.archives.pl

DOI: https://doi.org/10.24425/ams.2026.158820

JILIANG KAN[1,2*], KUN XIAO[2], KUNYOU ZHOU[2],
TONG WANG[2], JIAZHUO LI[2], LINMING DOU[3]

EXPERIMENTAL AND NUMERICAL INVESTIGATION ON DYNAMIC FAILURE AND ENERGY DISSIPATION OF SANDSTONE UNDER COUPLED STATIC-DYNAMIC LOADING

Catastrophic failures in underground rock engineering caused by coupled static-dynamic stresses result in economic losses and safety hazards globally. Quantifying rock dynamic failure and energy dissipation under such conditions is essential for mitigating geotechnical risks. This study employed modified split Hopkinson pressure bar (SHPB) experiments to perform coupled static-dynamic compression tests on sandstone under varying loading circumstances. A novel PFC-FLAC coupling methodology was developed to simulate real-time dynamic failure evolution of rock. Compared to uniaxial impact tests, more prominent phenomena of pre-peak plastic deformation stage and post-peak strain rebound are observed in the stress-strain curves of sandstone under coupled static-dynamic compression tests. The mechanical properties of sandstone are directly influenced by both dynamic stress and static stress (axial-confining pressure). Energy serves as the fundamental driving force of rock damage, and the dissipated energy has a considerable positive correlation with rock damage. Furthermore, fractal analysis quantitatively revealed progressive failure modes: local damage transitions to axial splitting and ultimately macroscopic crushing with increasing impact pressure. Crucially, elevated axial pressure accelerates impact-induced failure, while confining pressure systematically mitigates damage intensity. Post-failure analysis identified some specimens retaining structural integrity through circular platform cores with arched fracture surfaces. The failure mode is X-type conjugated failure caused by shear failure, which was verified by numerical simulations. These findings provide critical design parameters for predicting rock bursts in deep mining excavations and evaluating tunnel stability during blasting operations.

Keywords: Coupled static-dynamic loading; SHPB; sandstone; energy dissipation; failure mode

1 ANHUI UNIVERSITY OF SCIENCE AND TECHNOLOGY, ENGINEERING LABORATORY FOR SAFE AND PRECISE COAL MINING, CHINA
2 ANHUI UNIVERSITY OF SCIENCE AND TECHNOLOGY, SCHOOL OF MINING ENGINEERING, CHINA
3 CHINA UNIVERSITY OF MINING AND TECHNOLOGY, SCHOOL OF MINES, CHINA

* Corresponding author: jlkan@aust.edu.cn

1. Introduction

As mining operations and tunnel excavations advance deeper into the earth's strata, dynamic rock failures induced by high in-situ stresses coupled with strong dynamic disturbances have escalated significantly. These events present major threats to both the safety of miners and the stability of production [1,2]. Typical dynamic disasters such as rock bursts and roof collapses are frequently accompanied by intense mine seismicity and violent ejection of surrounding rock masses in underground roadways [3,4]. Fig. 1 illustrates the typical environmental conditions and triggering mechanisms of these phenomena. The removal of coal breaks the initial equilibrium of the three-dimensional stress state, which leads to the stress carried by the roof being transferred to the adjacent surrounding rock. This stress redistribution generates abutment pressures reaching approximately three to fourfold the original overburden stress, propagating progressively with mining advancement [5]. Moreover, the dynamic disturbances caused by mining seismicity, blasting operations, and hydraulic fracturing are not negligible and significantly contribute to the dynamic disasters [6,7]. Consequently, accurate quantification of dynamic failure characteristics and energy dissipation mechanisms in rock under coupled static-dynamic loading has become critically important, which can provide important guidance for the prediction and prevention of rock dynamic disasters.

The SHPB technique has been extensively utilised to investigate the dynamic behaviour of rock materials subject to impact pressure [8,9]. While uniaxial dynamic compression tests have yielded significant insights into rock mechanics [10-13], they inadequately replicate the complex three-dimensional stress states encountered in underground environments. Consequently, modified SHPB systems capable of applying simultaneous axial and confining pressures have been developed for coupled static-dynamic testing. Ma et al. [14] studied the dynamic mechanical responses of rock under coupling loading and found that static pre-stress will significantly affect the rock dynamic strength. Impact tests on sandstone under varying axial prestressed loading were conducted by Zhou et al. [15]. They discovered that the sandstone specimens were increasingly broken as static pre-stress increases, and the failure mechanism developed from tensile-dominated mixed to shear/tensile equivalent mode. Yang et al. [16] studied the energy dissipation characteristics of coal samples under various impact conditions and pointed out that the initial static energy accumulated in coal samples was inversely proportional to the energy required for their impact failure. Based on the SHPB equipment and PFC discrete element method, Luo et al. [17] analysed the change process of sandstone failure mode under different strain rates. Shen et al. [18] found that triaxial loading reduces the coal damage, but the maximum principal stress and impact pressure aggravate coal damage. Feng et al. [19] and Wu et al. [20] conducted the SHPB tests on the fissured rock and heat-treated rock to understand their mechanical properties and failure modes. Moreover, using the numerical models, including the finite element, discrete element, and finite-discrete coupling model, to simulate SHPB tests was widely accepted [21,22]. These numerical models can better reproduce the crack propagation and dynamic failure of rock samples during the impact. Based on FLAC and PFC codes, Liu et al. [23] established a continuous-discrete coupling numerical model to understand the dynamic mechanical behaviours of multi-jointed rock and discussed its influencing factors. Han et al. [24] and Liu et al. [25] also established SHPB numerical models to explore the impact failure of rock samples containing holes and intersecting jointed rock, and obtained some new beneficial findings. Fukuda, D et al. [26] developed a 3D hybrid finite-discrete element simulator to investigate rock fracturing under quasi-static and dynamic loading conditions. The results demonstrate that

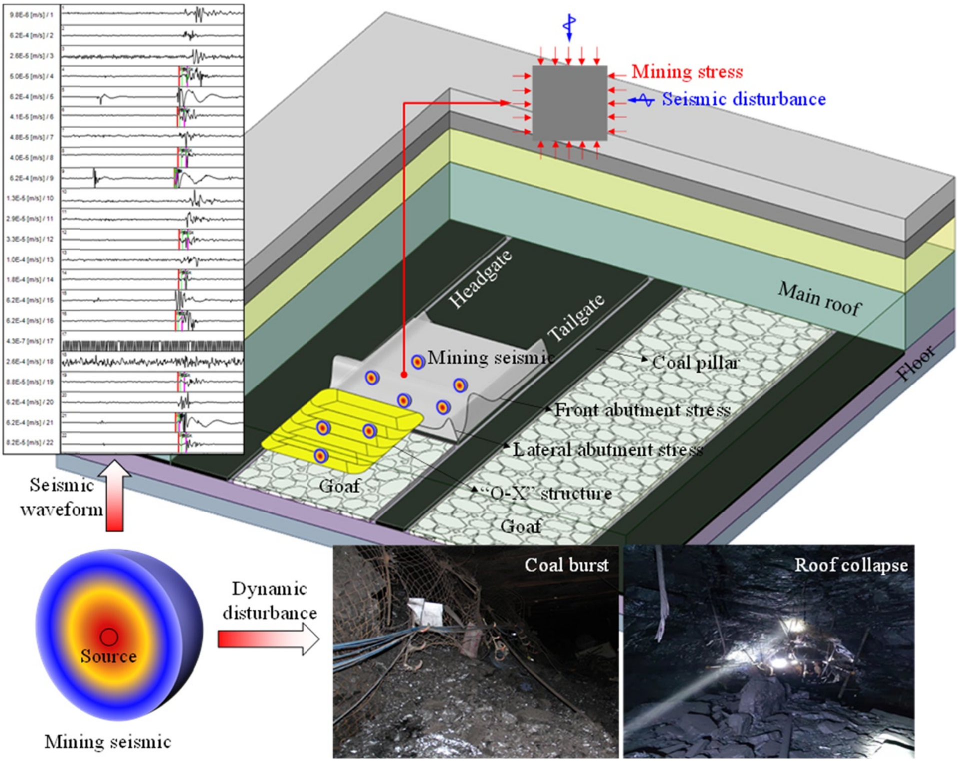

Fig. 1. Occurrence of the environment and inducing factors of dynamic disasters in underground coal mines

the simulator is a valuable and powerful numerical tool that is highly valuable in addressing problems related to rock mechanics engineering.

In underground coal mining operations conducted at depths exceeding 600 m, an environment particularly prone to dynamic disasters such as rock bursts and roof collapses, the rock structure generally suffers from static stress concentrations ranging from 15 MPa to 40 MPa. Given this critical high-static-stress loading environment, accurately characterising the rock's transient dynamic response to external disturbances, along with its macroscopic fracture propagation behaviour, is of paramount engineering significance for disaster prevention. However, engineering practice currently relies on limited empirical guidance due to the scarcity of high-fidelity impact tests on sandstone under true high-static prestress conditions. Existing experimental databases regarding dynamic failure evolution mechanisms under coupled high axial/confining pressures remain critically insufficient, and these data are in high demand for preventing dynamic disasters.

To address these engineering challenges, this research employed a modified SHPB equipment with triaxial pressure chambers to execute controlled coupled static-dynamic compression tests on sandstone specimens. The mechanical properties and energy dissipation characteristics of sandstone under different impact loading circumstances were first analysed. Subsequently, the fractal dimension analysis of post-failure debris was conducted, and the relationships between the fractal dimension and damage degree, impact pressure and static pre-stress were discussed. Finally, a PFC-FLAC hybrid computational model was developed to reconstruct real-time crack network evolution during coupled static-dynamic impact, and its failure modes and mechanisms were further revealed. The research findings will provide guidance for predicting and controlling rock dynamic hazards during deep mining operations and the excavation of deeply buried tunnels.

2. Material and methodology

2.1. Specimen processing and statics parameter testing

The raw sandstone was taken from the roof strata above the 6-1# coal seam at Dongxia coal mine, Gansu Province, China. Then, the drilling, slicing, and polishing procedures were performed successively to obtain the cylindrical specimens. To mitigate specimen heterogeneity effects on experimental results, all samples originated from a single rock block, ensuring consistent lithology and mechanical properties. Specimens were visually confirmed to be homogeneous and free of macroscopic cracks. Following the experimental standard stipulated by the international society for rock mechanics and rock engineering (ISRM) [9], the specimens with dimensions of Φ50×25 mm and Φ50×100 mm were prepared for testing. The uniaxial compression tests on three Φ50×100 mm specimens yielded the static mechanical parameters. The results indicated that the uniaxial compressive strength measured was 58.31, 61.92 and 63.24 MPa, and the elastic modulus was 9.4, 9.4 and 9.9 GPa, respectively (Fig. 2). The mean uniaxial compressive strength was 61.6 MPa, with an average Young's modulus of 9.6 GPa. This mechanical consistency validates specimen homogeneity and provides a reliable foundation for subsequent dynamic experiments.

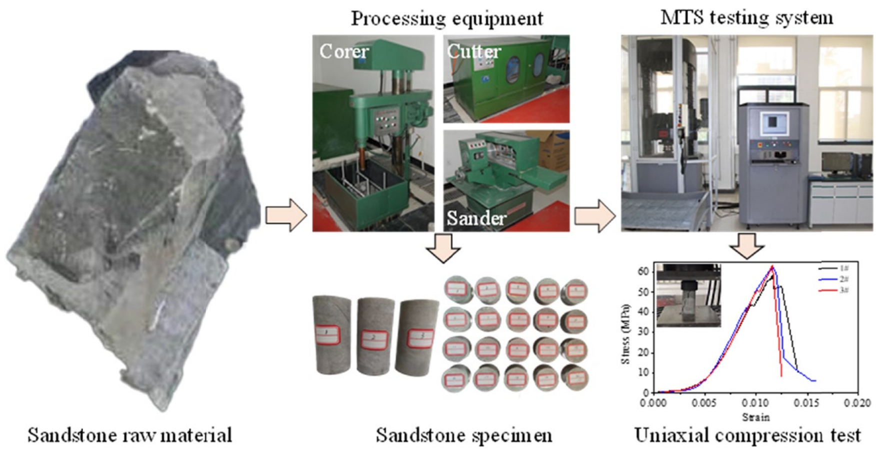

Fig. 2. Preparation of sandstone specimens and testing of static mechanics parameters

2.2. SHPB testing setup and data processing

The coupled static-dynamic impact tests were performed on sandstone specimens using the modified 50 mm-diameter SHPB equipment with axial and confining loading systems (Fig. 3). The components of the system include SHPB bars, impact loading subsystem, dynamic strain measuring subsystem, axial and confining pressure loading subsystem. The incident and transmission bars, both with a length of 2500 mm, were crafted from 60Si2MnA high-strength alloy steel. The strain gauges G1 and G2 affixed to the SHPB bars were employed to capture and record pulse signals. This configuration achieves maximum static prestress levels of 50 MPa in both axial and circumferential directions, effectively simulating in-situ deep-mining stress conditions for rock specimens.

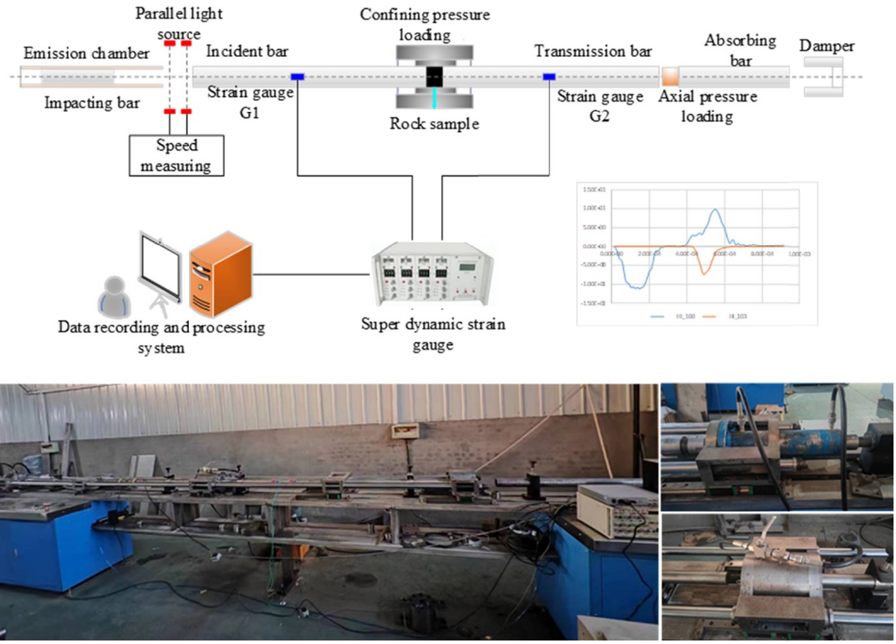

Fig. 3. The modified SHPB equipment with axial and confining loading system

Based on one-dimensional assumption and stress uniformity assumption, the strain rate $\dot{\varepsilon}$, strain ε and stress σ can be determined by analyzing the voltage data recorded by G1 and G2 strain gauges [27].

$$\begin{cases} \dot{\varepsilon}(t) = \dfrac{C_0}{L}\left[\varepsilon_i(t) - \varepsilon_r(t) - \varepsilon_t(t)\right] \\ \varepsilon(t) = \dfrac{C_0}{L}\displaystyle\int_0^t \left[\varepsilon_i(t) - \varepsilon_r(t) - \varepsilon_t(t)\right] dt \\ \sigma(t) = \dfrac{A_0 E_0}{2A_s}\left[\varepsilon_i(t) + \varepsilon_r(t) + \varepsilon_t(t)\right] \end{cases} \tag{1}$$

where A_0 and A_s are the cross-sectional area of the SHPB bar and sandstone specimen, respectively; E_0 and C_0 are Young's modulus and P-wave velocity; L is the sample length. The subscripts i, r and t represent the incident, reflected, and transmitted signals, respectively.

The aforementioned SHPB data processing method is commonly referred to as the three-wave method. Further, it is assumed that the strain and stress of the specimen are evenly distributed, then:

$$\varepsilon_i(t) + \varepsilon_r(t) = \varepsilon_t(t) \tag{2}$$

Eq. (1) can be modified as [28]:

$$\begin{cases} \dot{\varepsilon}(t) = -2\dfrac{C_0}{L}\varepsilon_r(t) \\ \varepsilon(t) = -2\dfrac{C_0}{L}\int_0^t \varepsilon_r(t)\,dt \\ \sigma(t) = \dfrac{A_0 E_0}{A_s}\varepsilon_t(t) \end{cases} \tag{3}$$

The energy carried by different waves in SHPB test can be described as [29,30]:

$$\begin{cases} W_I = \dfrac{A_0 C_0}{E_0}\int_0^t \sigma_i^2(t)dt \\ W_R = \dfrac{A_0 C_0}{E_0}\int_0^t \sigma_r^2(t)dt \\ W_T = \dfrac{A_0 C_0}{E_0}\int_0^t \sigma_t^2(t)dt \end{cases} \tag{4}$$

Assuming the scattering of stress waves and their energy dissipation are ignored, the energy absorbed by specimens is calculated as W_d:

$$W_d = W_I - W_R - W_T \tag{5}$$

Then, the dissipated energy density U_d is calculated as follows.

$$U_d = \frac{W_d}{V_s} \tag{6}$$

where, V_s is the specimen volume.

2.3. Testing procedure

Firstly, uniaxial impact tests with different impact pressures were performed for three sandstone specimens (A1~A3) in the A-series. Then, three series of coupled static-dynamic impact tests were conducted to investigate the dynamic mechanics behaviours of sandstone. The detailed loading parameters were listed in TABLE 1. The sandstone samples used in the SHPB tests measured Φ50×25 mm in dimension.

TABLE 1

Testing scheme parameters

<table>
<tr><th>Specimen loading diagram</th><th>Series No.</th><th>Specimen number</th><th>Axial pressure/MPa</th><th>Confining pressure/MPa</th><th>Impact pressure/MPa</th></tr>
<tr><td rowspan="3">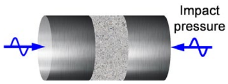
</td><td rowspan="3">A</td><td>1</td><td>0</td><td>0</td><td>0.4</td></tr>
<tr><td>2</td><td>0</td><td>0</td><td>0.6</td></tr>
<tr><td>3</td><td>0</td><td>0</td><td>0.8</td></tr>
<tr><td rowspan="15">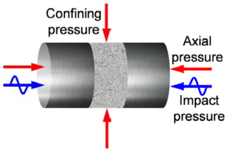
</td><td rowspan="5">B</td><td>1</td><td>25</td><td>20</td><td>0.4</td></tr>
<tr><td>2</td><td>25</td><td>20</td><td>0.6</td></tr>
<tr><td>3</td><td>25</td><td>20</td><td>0.8</td></tr>
<tr><td>4</td><td>25</td><td>20</td><td>1.0</td></tr>
<tr><td>5</td><td>25</td><td>20</td><td>1.2</td></tr>
<tr><td rowspan="5">C</td><td>1</td><td>10</td><td>5</td><td>1.0</td></tr>
<tr><td>2</td><td>15</td><td>5</td><td>1.0</td></tr>
<tr><td>3</td><td>20</td><td>5</td><td>1.0</td></tr>
<tr><td>4</td><td>25</td><td>5</td><td>1.0</td></tr>
<tr><td>5</td><td>30</td><td>5</td><td>1.0</td></tr>
<tr><td rowspan="5">D</td><td>1 (Same as C4)</td><td>25</td><td>5</td><td>1.0</td></tr>
<tr><td>2</td><td>25</td><td>10</td><td>1.0</td></tr>
<tr><td>3</td><td>25</td><td>15</td><td>1.0</td></tr>
<tr><td>4 (Same as B4)</td><td>25</td><td>20</td><td>1.0</td></tr>
<tr><td>5</td><td>25</td><td>25</td><td>1.0</td></tr>
</table>

3. Experimental results

3.1. Dynamic stress equilibrium

One-dimensional assumption and stress uniform assumption require a balanced stress state at both ends of the rock specimen, which is essential for the reliability of the test results. Fig. 4 presents the impact signals and the stress equilibrium results of specimens subjected to both uniaxial impact and coupled static-dynamic impact. The total of the incident and reflected signals closely aligns with the transmission signal under two loading conditions, suggesting the stress equilibrium requirement was satisfied. Consequently, the two-wave analysis method remains theoretically applicable, confirming the experimental data's validity for quantifying dynamic rock behaviour.

3.2. Dynamic mechanical behaviour of sandstone

Fig. 5 presents stress-strain curves along with the ultimate failure states of sandstone specimens under uniaxial impact and coupled static-dynamic impact with different impact pressures, revealing three characteristic deformation stages. The initial elastic stage exhibits linear stress-strain progression with negligible damage, transitioning to a plastic stage featuring decelerated stress increase and microcrack initiation. The failure stage manifests through progressive crack propagation and stress reduction culminating in structural collapse, with critical divergence

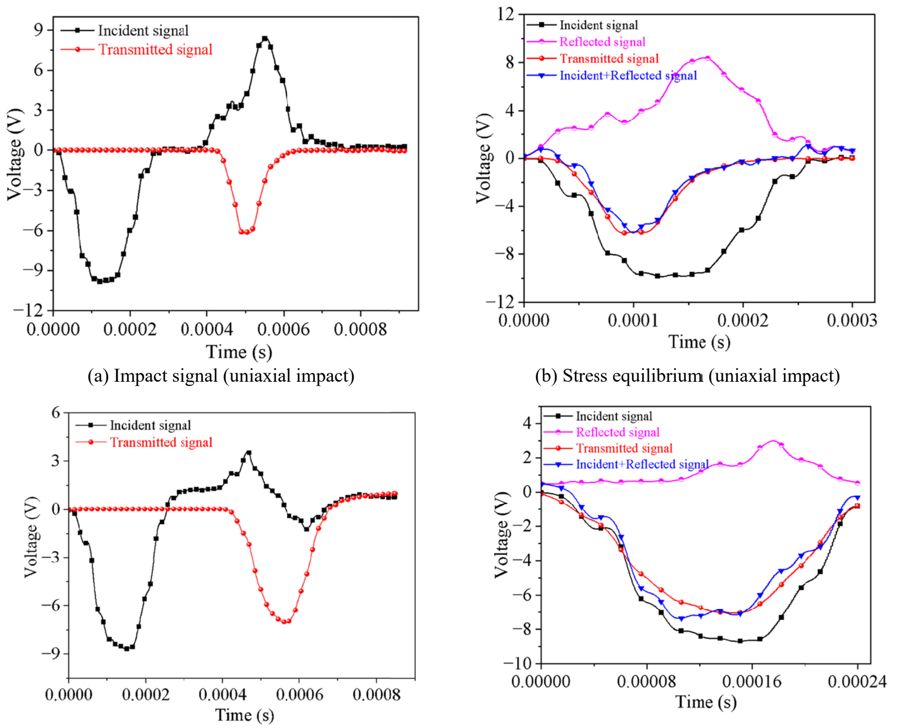

(a) Impact signal (uniaxial impact)
(b) Stress equilibrium (uniaxial impact)
(c) Impact signal (coupled static-dynamic impact)
(d) Stress equilibrium (coupled static-dynamic impact)

Fig. 4. Typical impact signals and stress equilibrium of tested specimens

observed under different loading modes. Specifically, coupled static-dynamic tests demonstrate post-peak strain rebound signifying residual load-bearing capacity and incomplete strain energy dissipation.

For uniaxial impact, dynamic mechanical parameters show pronounced strain-rate dependence. For uniaxial impact, the dynamic mechanical parameters of sandstone are significantly related to the strain rate. The dynamic strength improves from 235 MPa to 380 MPa when the impact pressure increases from 0.4 MPa to 0.8 MPa. Likewise, the elastic modulus follows a similar trend of variation. The sandstone specimens are completely destroyed after uniaxial impact and present in the form of small fragments and powder. Furthermore, as impact pressure increases, the fragment size decreases and the powder percentage increases, indicating increasingly severe rock damage.

For coupled static-dynamic impact, the pre-peak plastic deformation stage in the stress-strain curve was prominent, showing an approximate platform segment, and the strain rebound phenomenon manifests in the post-peak stage. Moreover, as the impact pressure increases, both the platform segment and the strain rebound phenomenon become increasingly obvious. Observing the failure state of the specimens after impact, at impact pressures of 0.4 MPa and 0.6 MPa, only slight cracks occurred on the local surface of specimens (B1 and B2), but no macroscopic fragmentation occurred. However, at an impact pressure of 0.8 MPa, the specimen (B3) broke along the axial direction, and both sides of the fracture were presented as complete blocks. Then, when the impact pressure increases to 1.0 MPa and 1.2 MPa, it can be found that the specimens (B4 and B5) were impacted into multiple fragments, and its main body showed a circular table shape. Moreover, the specimen B5 suffered more severe damage than that of specimen B4, mainly showing a larger number and a smaller size of fragments. Judging from the failure state of sandstone specimens, as impact pressure increases, the failure mode of the specimen will undergo a remarkable transformation, starting from local damage, progressing to axial splitting, and ultimately resulting in macroscopic crushing failure.

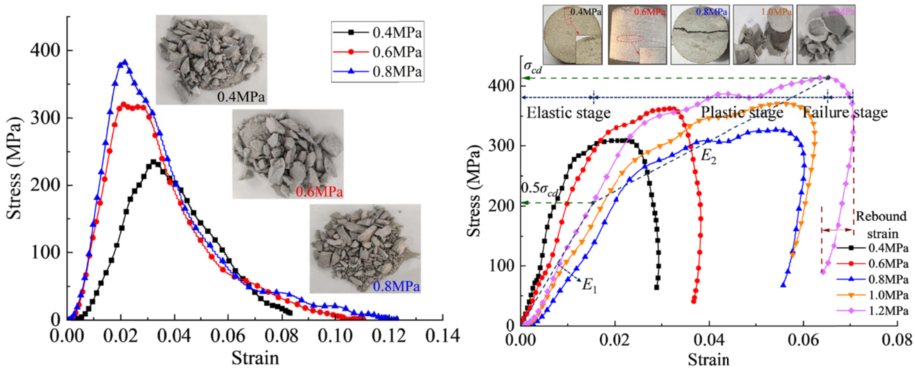

Fig. 5. Stress-strain curves and ultimate failure state of sandstone specimens

Fig. 6 presents dynamic mechanical parameters of sandstone specimens (including dynamic strength, elastic modulus E_1, plastic modulus E_2, and plastic strain) across varying impact pressures. The E_1 is defined as the slope between the origin and 50% dynamic strength ($0.5\sigma_{cd}$), and E_2 represents the slope between $0.5\sigma_{cd}$ and σ_{cd} [31], while plastic strain corresponds to the strain during plastic deformation. Overall, the dynamic strength of sandstone specimens does not strictly follow the trend of increasing with the impact pressure. In particular, in this test, the dynamic

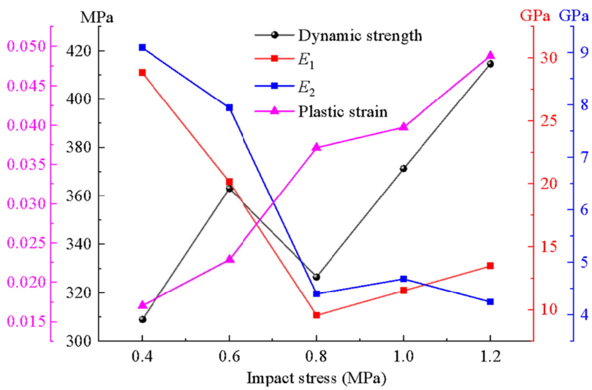

Fig. 6. Dynamic mechanical parameters of sandstone in B series impact tests

strength experiences a sudden decrease when the impact pressure reaches 0.8 MPa, and then re-increases with the impact pressure. Similarly, both E_1 and E_2 exhibit an initial decrease and then an increase as the impact pressure increases. Conversely, the plastic strain gradually increases with impact pressure, which determines the increasing damage degree of the sandstone specimen.

As the fundamental driver of rock failure, energy evolution during impact critically governs fracture mechanisms. Fig. 7 quantifies energy distribution proportions in SHPB tests under uniaxial and coupled static-dynamic loading. All types of energy exhibit an increasing tendency when the impact pressure increases. During uniaxial impact testing, the reflected energy accounts for approximately 45-50% of incident energy, while transmitted energy comprises merely 20%. This trend reverses fundamentally under coupled static-dynamic loading. This is because the specimen was broken into smaller fragments, subjected to uniaxial impact, where most of the energy was reflected and absorbed for crack expansion. However, the strength of sandstone specimens improves dramatically under static axial and confining pressure loading, as does their capacity to resist impact crushing damage, resulting in more energy being transferred to the transmission bars. Notably, when the sandstone specimen changes from local damage to axial splitting, the percentage of transmitted energy decreases significantly (from 62.5% to 41.0%), while the percentage of dissipated energy increases significantly (from 28.0% to 42.3%).

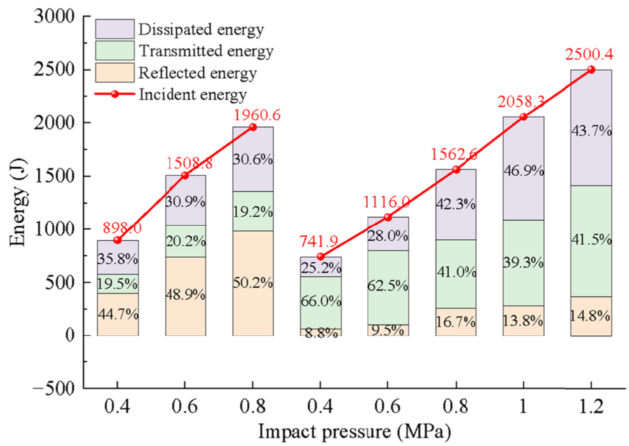

Fig. 7. Energy distribution during the impact of sandstone specimens

3.3. Influence of static pre-stress on impact characteristics of sandstone

Fig. 8 presents stress-strain curves and mechanical parameters of sandstone under coupled static-dynamic impact at differing axial pressures (specimens C1-C5). The stress-strain curves are similar in shape, and strain rebound happens. Under the constant confining pressure and impact pressure, increasing axial pressure reduces dynamic strength from 433.00 MPa to 390.60 MPa, decreases elastic modulus E_1 and plastic strain, while increasing plastic modulus E_2. Moreover, all specimens have serious macroscopic damage, and the specimens exist in the form of a circular platform with some fragments. Among them, the main body of the C1, C4 and C5 specimens was fractured accompanied by numerous small fragments, while the main body of the C2 and C3 specimens remained relatively intact. Overall, the sandstone damage degree presents a tendency of first decreasing and then increasing. Mechanistically, low axial pressure prevents premature failure by compacting internal fissures and enhancing mechanical properties, thereby increasing the critical impact energy threshold for fracture propagation. Conversely, elevated axial pressure reduces the failure energy barrier. Furthermore, high axial pressure promotes stored strain energy release that drives additional fracture propagation.

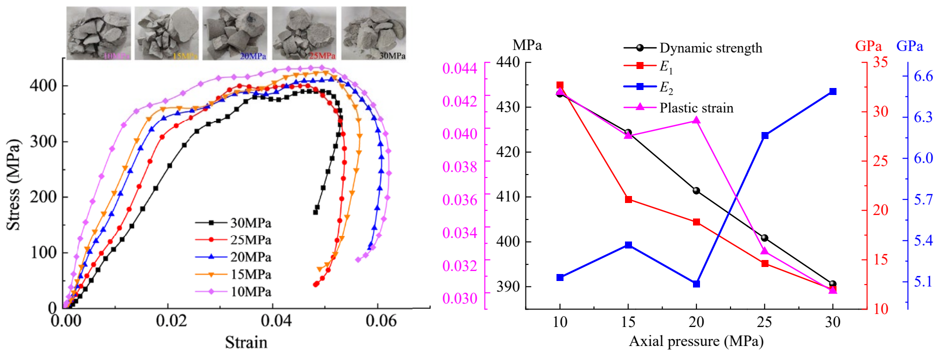

(a) Stress-strain curves (b) Mechanical parameters

Fig. 8. Stress-strain curves and mechanical parameters of sandstone specimens in C series impact tests

Fig. 9 depicts energy partitioning in sandstone specimens (C1-C5) during impact testing. Under constant impact pressure, the incident energy attenuates linearly with increasing axial pressure, consistent with the incident wave amplitude reduction observed under axial stress by

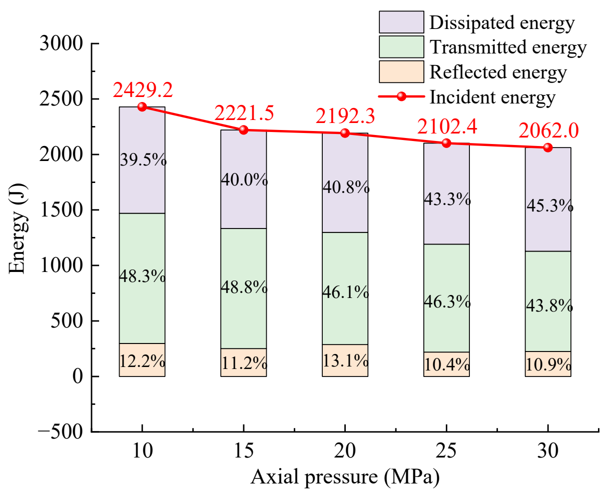

Fig. 9. Energy distribution of specimens under different axial pressure during the impact process

Jin et al. [32]. In this series of tests, the transmitted and dissipated energy account for the majority, with an average of 46.7% and 41.8%, respectively, while the reflected energy accounts for a smaller proportion, amounting to only 11.6%. Notably, the percentage of dissipated energy increases with axial pressure, whereas transmitted energy decreases proportionally. The formation of smaller rock fragments requires more energy to be absorbed for fracture propagation. Therefore, when the damage to sandstone intensifies, the percentage of dissipated energy increases progressively.

Fig. 10 presents the stress-strain curves and mechanical parameters of sandstone under coupled static-dynamic impact with various confining pressure loading schemes (D1-D5). Overall, the dynamic strength of sandstone increases from 400 MPa to 460 MPa with rising confining pressure (excepting D4 at 371 MPa), while the plastic strain decreases. Moreover, there is no discernible change in the law of deformation modulus E_1 and E_2. The damage evolution of sandstone exhibits significant confining-pressure dependence. The sandstone specimens D1 and D2 have suffered serious macroscopic failure, D3 and D4 display localised failure with large fragment spalling, and D5 maintains structural integrity with minor boundary damage. The impact resistance of rock specimens was enhanced, and the rock damage gradually weakened as the confining pressure increased. The formation and expansion of cracks are limited by confining pressure during rock impact failure, which is hindered by the impact failure of the specimen. Furthermore, the variations in the levels of damage among the specimens with various confining pressures demonstrated that confining pressure has a bigger impact on specimen failure than axial pressure.

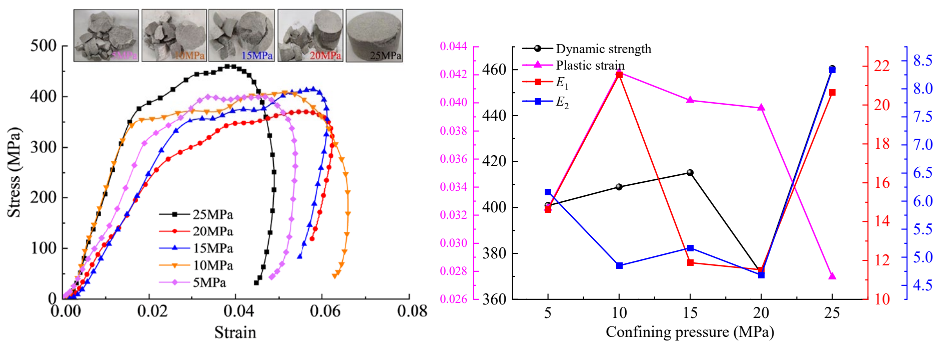

(a) Dynamic stress-strain (b) Mechanical parameters

Fig. 10. Stress-strain curves and mechanical parameters of sandstone specimens in D series impact tests

Fig. 11 shows the energy distribution of sandstone specimens (D1 to D5) during the impact process. Provided that both the impact and axial pressures remain constant, the incident energy remains unchanged irrespective of variations in the confining pressure. In this group of tests, the transmitted energy accounts for the majority, and its percentage increases with the confining pressure, while that of dissipated energy exhibits the opposite change law. Especially, the transmission energy ratio of the D5 specimen can reach 57.5%, and the dissipated energy ratio was only 33.9%. From the perspective of energy dissipation, the constraining influence of confining pressure on rock impact failure can be further explained.

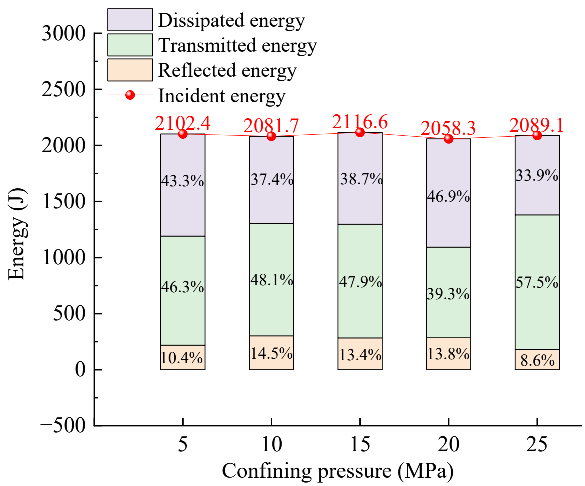

Fig. 11. Energy distribution of specimens under different confining pressure during the impact process

3.4. Fractal characteristics of rock fragments after impact failure

Fractal theory has been widely used in many research fields of rock mechanics. Existing studies have demonstrated that the rock fragment distribution after impact failure has good fractal characteristics, and the fractal dimension can quantify the crushing effect of rock [33-35]. Therefore, the rock fragments were collected and divided into seven levels according to their size, which were <1 mm, 1~5 mm, 5~10 mm, 10~15 mm, 15~25 mm, 25~40 mm, and >40 mm. Notably, the small fragments and powders of sandstone specimens after impact failure were not fully collected, and the weight of the collected fragments was less than the initial weight of the specimen. Especially for the specimens subjected to the uniaxial impact, only 50%~65% of the weight of fragments can be collected. To mitigate resultant calculation errors, uncollected material was assumed to comprise particles <1 mm. The screening results of rock fragments in each group of tests are listed in TABLE 2. Overall, the cumulative weight of small fragments increases with the impact pressure, while the axial and confining pressures have different effects.

The fractal dimension was calculated to better quantify the rock failure characteristics. The particle size distribution equation of rock fragment size was explained by the weight-size relationship in fractal geometry as follows [36,37].

$$y = \frac{M_r}{M_t} = \left(\frac{r}{r_m}\right)^{3-D} \tag{7}$$

where r is rock fragment size, r_m is the maximum size of the rock fragment; M_r is the cumulative weight of the fragments less than r; M_t is the total weight of the fragments.

Eq. (7) was transformed logarithmically:

$$\ln y = \ln\left(\frac{M_r}{M_t}\right) = (3-D)\left(\frac{r}{r_m}\right) \tag{8}$$

The fractal parameters of the sandstone specimens B-1, B-2, and D-5 cannot be determined because there has not been any macroscopic failure in them. Therefore, the fractal dimension of these specimens was set to zero in this research. For the other fractured rock specimens, the relationship between the weight and size was established in the coordinates of $\ln(M_r/M_t) - \ln(r/r_m)$, as depicted in Fig. 12. These exhibit strong linearity with fitting coefficients $R^2 \geq 0.9$, confirming fragment self-similarity. Furthermore, the fractal dimension D was derived from the slope of these regressions, with results documented in TABLE 2. Under uniaxial impact testing, the fractal dimension of the three sandstone specimens were recorded as 2.74, 2.82, and 2.85, respectively, while that of sandstone specimens under coupled static-dynamic impact ranged from 0 to 1.66. The significant difference in fractal dimension indicated that the sandstone specimens suffered from more serious crushing failure in uniaxial impact compression tests. Fig. 13 illustrates the relationship between the fractal dimension of the specimen fragment and the impact pressure, axial pressure and confining pressure. As the impact pressure intensifies, the fractal dimension initially undergoes a gradual ascent from 0 to 0.22, followed by a rapid surge reaching 1.0 and culminating at 1.59. This rapid increase signifies more severe damage and fragmentation of sandstone specimens. The fractal dimension exhibits a biphasic behaviour with respect to axial pressure, initially declining and subsequently rising as the pressure intensifies. Conversely, it undergoes a steady decrease as the confining pressure increases. Through comparative analysis of failure modes of sandstone samples, it is concluded that a higher fractal dimension correlates directly with a more severe degree of rock failure.

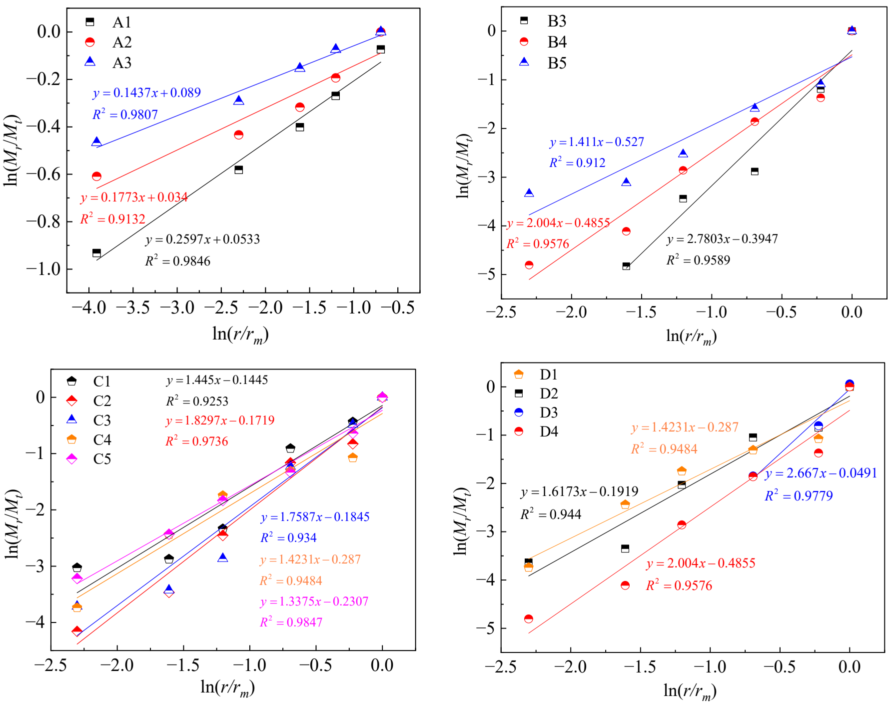

(c) Series C (d) Series D

Fig. 12. $\ln(M_r/M_t) - \ln(r/r_m)$ relationship for each group of fractured sandstone specimens

TABLE 2

Sieving results of sandstone specimen fragments and their fractal dimension *D*

No.	Specimen weight/g	Fragments weight/g							Fractal dimension D	Correlation coefficient
		<1 mm	1~5 mm	5~10 mm	10~15 mm	15~25 mm	25~40 mm	>40 mm		
A1	127	59	21	14	12	21	0	0	2.74	0.9846
A2	125	68	13	10	12	22	0	0	2.82	0.9132
A3	126	79	15	14	9	9	0	0	2.85	0.9807
B1	121	0	0	0	0	0	0	121	0	—
B2	119	0	0	0	0	0	0	119	0	—
B3	125	0	0	1	3	2	31	88	0.22	0.9589
B4	122	0	1	1	5	12	12	91	1.00	0.9576
B5	114	2	3	1	4	14	15	75	1.59	0.912
C1	124	4	2	1	5	38	30	44	1.55	0.9253
C2	128	1	1	2	7	29	16	72	1.17	0.9736
C3	123	2	1	1	3	29	40	47	1.24	0.934
C4	126	2	1	8	11	12	9	83	1.58	0.9484
C5	125	3	2	6	6	16	33	59	1.66	0.9847
D1	126	2	1	8	11	12	9	83	1.58	0.9484
D2	114	1	2	1	11	25	9	65	1.38	0.944
D3	121	1	0	0	0	17	33	70	0.33	0.9779
D4	122	0	1	1	5	12	12	91	1.00	0.9576
D5	126	6	0	0	0	0	0	120	0	—

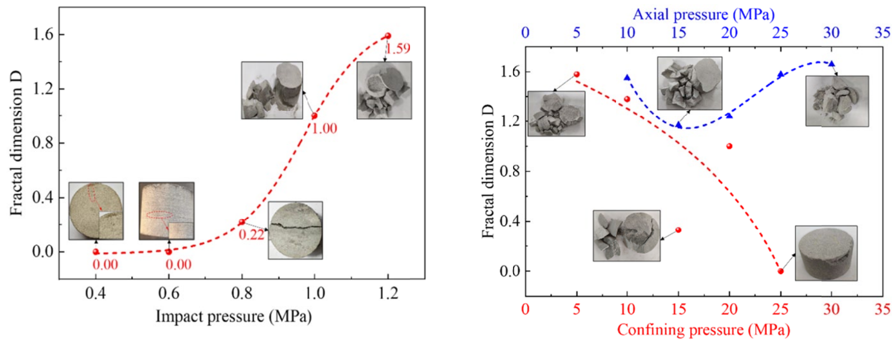

(a) Fractal dimension under different impact pressures

(b) Fractal dimension under different axial and confining pressures

Fig. 13. Fractal dimension of rock fragments

Fig. 14 presents a clear illustration of the correlation between energy dissipation density and fractal dimension during the impact process of sandstone. The analysis reveals a positive and significant association between these two parameters. Consequently, the energy dissipation density serves as an effective metric for quantifying the extent of damage in sandstone, where a heightened energy dissipation density corresponds to a more pronounced degree of sandstone fragmentation.

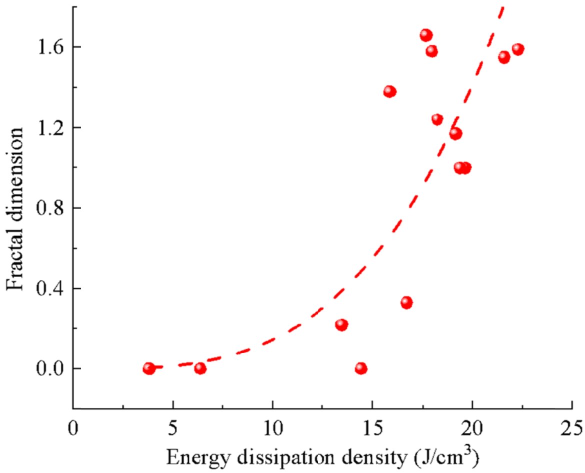

Fig. 14. Relationship between energy dissipation density and fractal dimension

4. Dynamic failure mechanism of sandstone

The typical failure modes of sandstone under coupled static-dynamic impact were presented in Fig. 15. Based on the macroscopic failure patterns observed after impact, the rock failure types can be categorised into three distinct groups. The first is a local failure mode; the main body of the sandstone specimen remains intact, there are circumferential cracks and through-axial cracks inside the rock, or there are particles peeling off the rock surface. The second is the "X" type conjugated failure mode, the sandstone fragments retain two conical bodies, and the fracture surface is curved. The third is the crushing failure mode, the sandstone suffered serious damage, and the fragments have no obvious main body. According to the aforementioned analysis, the failure mode of sandstone was affected by the interaction of impact pressure, axial pressure and confining pressure. Specifically, the sandstone specimens undergo axial compression deformation subjected to impact pressure, which subsequently leads to circumferential transverse deformation. However, due to the existence of friction and confining pressure on the end face of the sandstone specimens, the transverse expansion deformation will be limited, and the transverse tensile frac-

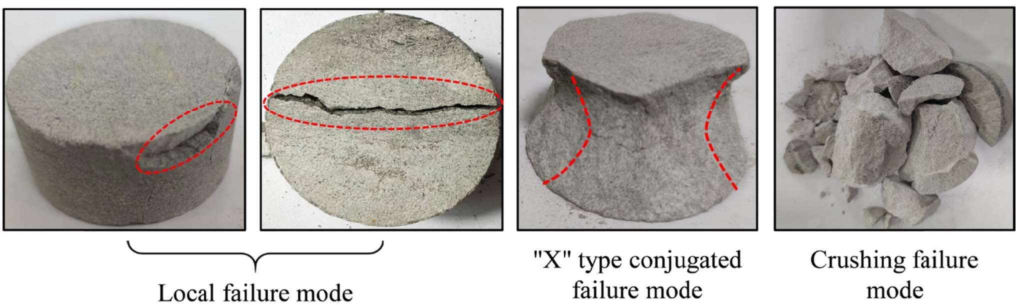

Fig. 15. Typical failure modes of sandstone under coupled static-dynamic impact

ture is not easy to occur. Meanwhile, the circumferential cracks appear closer to the core of the sandstone. Moreover, a large gap between axial impact pressure and confining pressure leads to a large shear stress. As a result, the bedding fault occurs in the sandstone, forming an inclined fracture surface at a certain angle to the axis, and finally appearing as two conical bodies. The sandstone specimens exhibit a mode of failure characterised by compressive shear failure when subjected to coupled static-dynamic impact.

While laboratory tests provide an intuitive assessment of rock dynamic mechanics, they lack real-time failure visualisation capacity. To overcome these shortcomings and gain deeper insights, numerical simulation techniques have emerged as a powerful tool in recent years, enabling researchers to explore such questions [38-40]. Therefore, to further understand the microscopic mechanism of sandstone under high strain rate, especially the real-time evolution of the failure process, the coupling method of PFC and FLAC was employed to simulate the dynamic failure of the sandstone specimen. As depicted in Fig. 16, the established numerical model incorporates two different components: the finite element part, which encompasses the incident and transmission bars, and the discrete element part, which represents the sandstone specimens. To ensure the numerical results match well with the laboratory tests, the parameters of the bars and specimens are designed to be exactly consistent with the laboratory tests. The lengths and diameters of bars are 2500 mm and 50 mm, respectively. Then, the bars are divided into 500, 20 and 5 parts in axial, peripheral and radial directions, respectively. The sandstone specimen is composed of 35252 particles, whose length and diameter are 25 mm and 50 mm, respectively. The radius of the particles varies within the range of 0.45mm to 0.75mm, and the parallel bonding model was adopted to simulate the fracture behaviour of rock [41]. A stress pulse was applied on the left end of the incident bar to simulate the impact of the bullet [17]. In this research, the stress pulse adopts the actual incident stress obtained by laboratory SHPB tests. Before the impact stress loading, the specimen underwent a static stress preload, characterised by an axial stress of 25 MPa and a circumferential stress of 20 MPa.

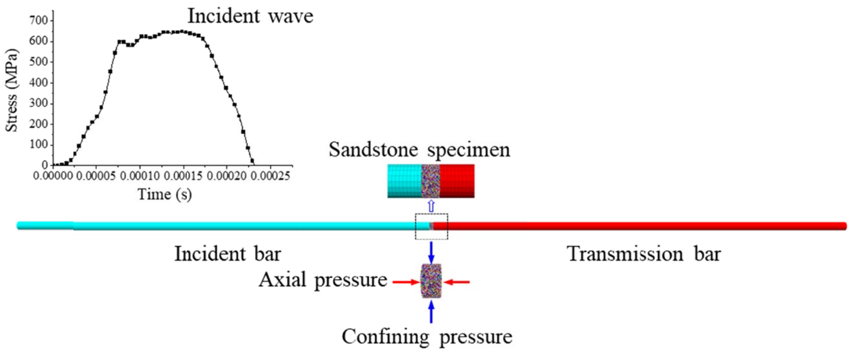

Fig. 16. The established SHPB numerical model

Based on the stress loading parameters of B4 and B5 sandstone specimens from the laboratory SHPB tests, the microscopic mechanical parameters of sandstone were calibrated through trial-and-error procedures to align with their macroscopic mechanical behaviour, as detailed in TABLE 3. Fig. 17 presents the stress-strain curves derived from both laboratory impact compression tests and numerical simulations. The good consistency of the two curves verifies the validity of the SHPB numerical model and parameters.

TABLE 3

Microscopic parameters of sandstone specimen

Type	Contact models	Radius/m	Density (kg/m^3)	*Emod* (GPa)	*Kratio*	*Pb_ten* (MPa)	*Pb_coh* (MPa)	*Pb_fa* (°)	Friction
Sandstone	Linearpbond	4.5×10^{-4}~ 7.5×10^{-4}	2700	4	3.0	165	105	30	0.6

Note: *Pb_ten*, *Pb_coh* and *Pb_fa* represent the tensile strength, cohesion and friction angle in the parallel bonding model, respectively.

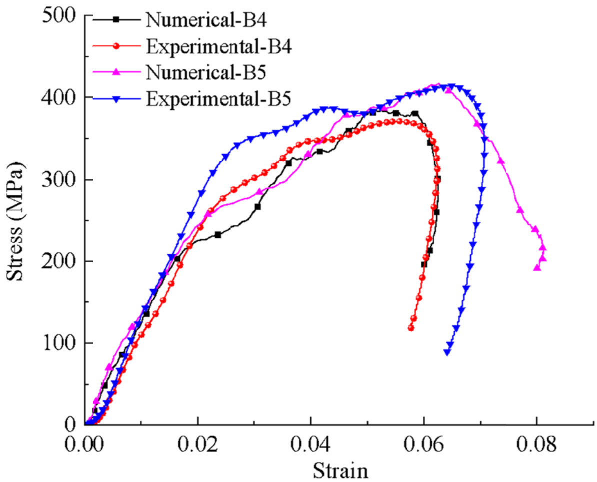

Fig. 17. Stress-strain curves derived from laboratory impact compression tests and numerical simulations

Fig. 18 depicts the evolution of internal cracks and force chains of sandstone specimens B4 and B5 under the coupled static-dynamic impact. As the impact stress waves are applied and propagate through the specimens, the wave-facing (left) side of the sandstone undergoes initial compression. Subsequently, once the stress wave passes the entire specimen, cracks begin to emerge. To be specific, sandstone specimens initially exhibit cracks emanating from their circumferential boundary and subsequently proliferate into numerous cracks along the left interface. As the impact stress wave permeates through the specimen, these cracks continually accumulate and progressively advance into its interior. Notably, the cracks occurred in the central region approach closer to the sandstone's core, consequently giving rise to a discernible angle between the fracture plane and the specimen's axial direction. Overall, the left side of the sample distinctly displays a substantially higher density and concentration of cracks compared to the right side. Furthermore, the distribution of contact forces within the sandstone's force chain initially intensifies as the impact stress improves. However, once the stress exceeds the yield strength of sandstone, the internal particle contact bonds are disrupted, leading to a marked reduction in the contact force of the force chain to a minimal level. The force chain's contact force steadily decreases and eventually stabilises when the impact loading gradually ends. Furthermore, it is evident that the spatial distribution of cracks aligns congruently with the contact force distribution of the force chain. By comparing the crack and force chain distribution of sandstone specimens under two impact pressures, the number of cracks, damage degree, and contact force of the force chain in sandstone specimens increase with the impact pressure.

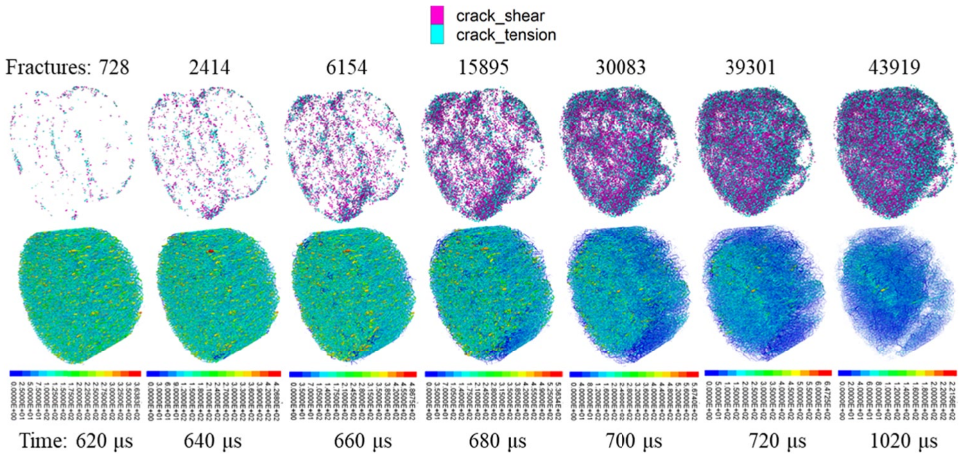

(a) Sandstone specimen B4

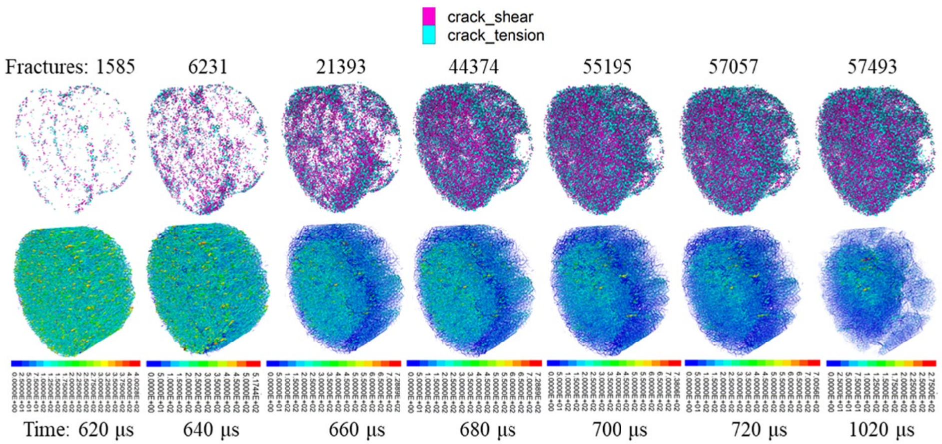

(b) Sandstone specimen B5

Fig. 18. Evolution of internal cracks and force chains of sandstone specimens

Fig. 19 presents the front view of the crack distribution in the sandstone specimen and the quantitative evolution of cracks. Notably, the circumferential boundary region of the specimen exhibits a lower density of cracks, predominantly characterised by tensile cracks. These cracks are caused by the tensile failure of the boundary particles during the initial stage of impact loading. Then, a significant number of cracks emerge within the intermediary zone between the boundary and the core of the specimen, and the fracture surface is a certain distance from the circumferential boundary of the specimen. Furthermore, from the front view of the specimen, it can be seen that there are relatively few cracks in the core of the specimen, indicating that the specimen is not completely destroyed and still retains a complete structure. Simultaneously, the internal fracture surfaces within the specimens exhibit an arcuate shape, indicative of a characteristic X-type conjugated failure mode, which aligns with laboratory test outcomes. Analysing the temporal correlation between crack proliferation and stress variation in the specimens, it is observed that cracks commence to manifest in specimens B4 and B5 when the respective stress thresholds of 225 MPa and 250 MPa are surpassed. Then, the cracks accumulate rapidly during the process of specimen stress growth to the peak. At the post-stress peak stage, cracks will continue to accumulate, but with the gradual reduction of stress, cracks gradually stop developing and eventually remain stable.

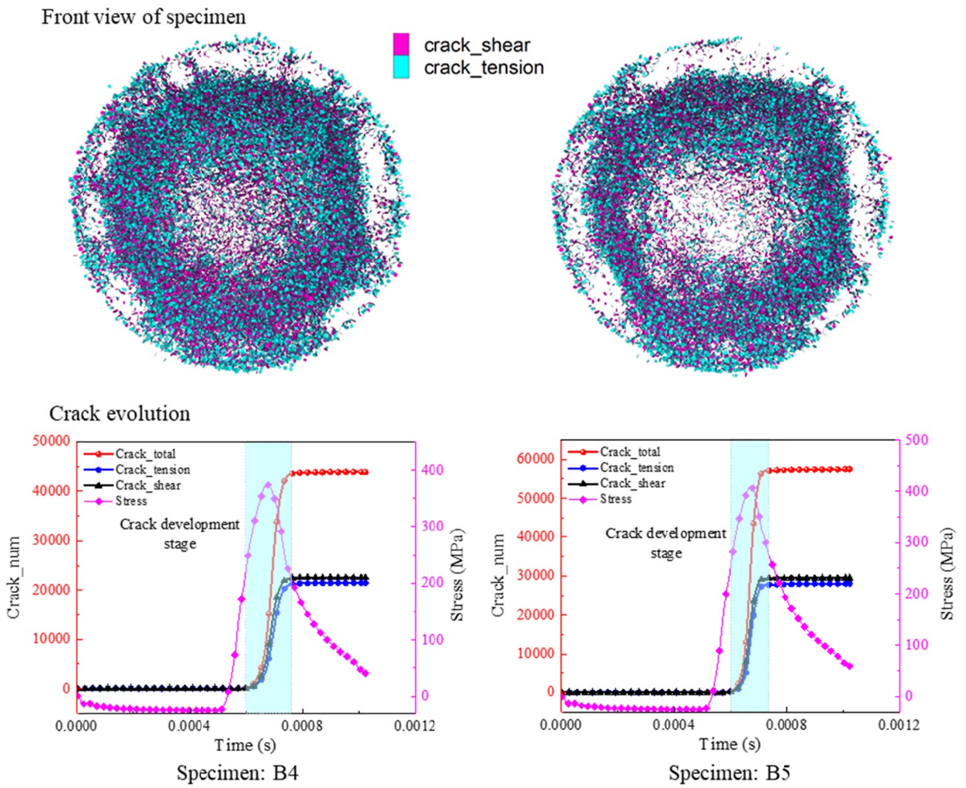

Fig. 19. Front view of crack distribution in sandstone specimens and the quantitative evolution of cracks

5. Conclusions

The laboratory tests and numerical simulations conducted in this study examined the dynamic mechanical parameters, failure modes, and energy dissipation characteristics of sandstone under coupled static-dynamic impact. The influences of impact pressure, axial pressure, and confining pressure on failure behaviour were systematically analysed. These findings provide an important basis for preventing rock dynamic failures in underground spaces. The main findings were as follows:

(1) The stress-strain curves of sandstone specimens exhibit notable differences when subjected to uniaxial impact and coupled static-dynamic impact. More prominent phenomena of pre-peak plastic deformation stage and post-peak strain rebound are observed in the stress-strain curve of sandstone under coupled static-dynamic impact tests. This indicated that the sandstone specimens after coupled static-dynamic impact still retain part of their dynamic bearing capacity after impact failure.

(2) The dynamic strength shows significant strain-rate dependency, increasing with impact pressure except for a temporary reduction at the 0.8 Mpa threshold. Both E_1 and E_2 demonstrate an initial decline followed by an increase, while the plastic strain gradually increases. Increasing axial pressure reduces dynamic strength, plastic strain, and E_1 while elevating E_2. Higher confining pressure enhances impact resistance through dynamic strength elevation and plastic strain suppression.

(3) In the coupled static-dynamic impacts, the energy percentage is highest in transmitted energy and lowest in reflected energy, while it is exactly the opposite in uniaxial impact tests. As impact pressure and axial pressure increase, the percentage of dissipated energy rises while that of transmitted energy drops. Additionally, as the confining pressure increases, the percentage of transmission energy rises, while that of dissipated energy shows the opposite change law.

(4) The rock fragment distribution after impact failure has good fractal characteristics. A positive correlation was observed among the impact damage degree, fractal dimension *D*, and the energy dissipation density of the sandstone specimens. The higher the damage degree of the sandstone sample, the larger the fractal dimension and the corresponding energy dissipation density.

(5) Failure modes transition progressively from localised damage through X-conjugated shear failure to macroscopic crushing with intensifying impact stress. The high axial pressure promotes the impact-induced failure in sandstone samples, while the rock damage gradually weakens as the confining pressure increases. Particularly, when macroscopic failure occurs in the specimen, its main body shows a circular table shape. This failure mode, characterised by an X-type conjugated failure pattern stemming from shear stress, has been verified through numerical simulations.

Funding

We gratefully acknowledge the financial support for this work provided by National Natural Science Foundation of China (No. 52504072, 52304197), the Scientific Research Foundation of High-level Talents of Anhui University of Science and Technology (No. 2023yjrc75), Engineering Laboratory for Safe and Precise Coal Mining of Anhui Province (No. ESCMP202401).

Data Availability Statement

The data presented in this study are available on request from the corresponding author.

Competing interests

The authors declare that they have no known competing financial interests or personal relationships that could have appeared to influence the work reported in this paper.

References

[1] Y.J. Chai, L.M. Dou, W. Cai, P. Małkowski, X.W. Li, S.Y. Gong, J.Z. Bai, J.R. Cao, Experimental investigation into damage and failure process of coal-rock composite structures with different roof lithologies under mining-induced stress loading. International Journal of Rock Mechanics and Mining Sciences **170**, 105479 (2023). DOI: https://doi.org/10.1016/j.ijrmms.2023.105479

[2] W. Pytel, B. Palac-Walko, J. Butra, P. Mertuszka, Friction stabilizers for rock bursts hazard mitigation in deep mines' environments. Tunnelling and Underground Space Technology **168**, 107096 (2025). DOI: https://doi.org/10.1016/j.tust.2025.107096

[3] L.P. Dai, Y.S. Pan, Z.H. Li, A.W. Wang, Y.H. Xiao, F.Y. Liu, T.W. Shi, W.H. Zheng, Quantitative mechanism of roadway rockbursts in deep extra-thick coal seams: Theory and case histories. Tunnelling and Underground Space Technology **111**, 103861 (2021). DOI: https://doi.org/10.1016/j.tust.2021.103861

[4] A. Tajdus, M. Cala, K. Tajdus, Seismicity and rock burst hazard assessment in fault zones: A case study. Archives of Mining Sciences **63** (3), 747-765 (2018). DOI: https://doi.org/10.24425/123695

[5] S.T. Ji, H. He, J. Karlovsek, Application of superposition method to study the mechanical behaviour of overlying strata in longwall mining. International Journal of Rock Mechanics and Mining Sciences **146**, 104874 (2021). DOI: https://doi.org/10.1016/j.ijrmms.2021.104874

[6] G.Y. Si, W. Cai, S.Y. Wang, X. Li, Prediction of Relatively High-Energy Seismic Events Using Spatial-Temporal Parametrisation of Mining-Induced Seismicity. Rock Mechanics and Rock Engineering **53** (11), 5111-5132 (2020). DOI: https://doi.org/10.1007/s00603-020-02210-3

[7] J. Dubinski, K. Stec, J. Krupanek, Comprehensive use of the Gutenberg–Richter law and geotomography for improving seismic hazard evaluation in hard coal mines. International Journal of Coal Science & Technology **10** (1), 3 (2023). DOI: https://doi.org/10.1007/s40789-022-00561-6

[8] Z.D. Smith, W.A. Griffith, Influence of preexisting damage on dynamic fragmentation behavior of sandstone. Journal of Structural Geology **199**, 105493 (2025). DOI: https://doi.org/10.1016/j.jsg.2025.105493

[9] Y.X. Zhou, K. Xia, X.B. Li, H.B. Li, G.W. Ma, J. Zhao, Z.L. Zhou, F. Dai, Suggested methods for determining the dynamic strength parameters and mode-I fracture toughness of rock materials. International Journal of Rock Mechanics and Mining Sciences **49**, 105-112 (2012). DOI: https://doi.org/10.1016/j.ijrmms.2011.10.004

[10] D.H. Ai, Y.C. Zhao, Q.F. Wang, C.W. Li, Crack propagation and dynamic properties of coal under SHPB impact loading: Experimental investigation and numerical simulation. Theoretical and Applied Fracture Mechanics **105**, 102393 (2020). DOI: https://doi.org/10.1016/j.tafmec.2019.102393

[11] S. Akdag, M. Karakus,G.D. Nguyen, A. Taheri, Q.B Zhang, J. Zhao, Dynamic response and fracture characteristics of thermally-treated granite under dynamic loading. International Journal of Rock Mechanics and Mining Sciences **170**, 105482 (2023). DOI: https://doi.org/10.1016/j.ijrmms.2023.105482

[12] M. Imani, H.R. Nejati, K. Goshtasbi, Dynamic response and failure mechanism of Brazilian disk specimens at high strain rate. Soil Dynamics and Earthquake Engineering **100**, 261-269 (2017). DOI: https://doi.org/10.1016/j.soildyn.2017.06.007

[13] F. Robbiano, K. Liu, Q.B. Zhang, L.F. Orellana, Dynamic uniaxial compression testing of veined rocks under high strain rates. International Journal of Rock Mechanics and Mining Sciences **153**, 105085 (2022). DOI: https://doi.org/10.1016/j.ijrmms.2022.105085

[14] Z.G. Ma, P.F. Yan, S.X. Cheng, P. Gong, F.Z. Qi, J.G. Wang, Experimental study of the dynamic mechanical responses and failure characteristics of coal under true triaxial confinements. International Journal of Mining Science and Technology **33** (6), 761-772 (2023). DOI: https://doi.org/10.1016/j.ijmst.2023.03.002

[15] Z.L. Zhou, X. Cai, X.B. Li, W.G. Cao, X.M. Du, Dynamic Response and Energy Evolution of Sandstone Under Coupled Static–Dynamic Compression: Insights from Experimental Study into Deep Rock Engineering Applications. Rock Mechanics and Rock Engineering **53** (3), 1305-1331 (2019). DOI: https://doi.org/10.1007/s00603-019-01980-9

[16] S. Yang, J.G. Ning, X.L. Zhang, J. Wang, X.S. Shi, X.Z. Qu, Determination of critical energy for coal impact fracture under coupled static-dynamic loading. Engineering Failure Analysis **160**, 108222 (2024). DOI: https://doi.org/10.1016/j.engfailanal.2024.108222

[17] Y. Luo, G. Wang, X.P. Li, T.T. Liu, A.K. Mandal, M.N. Xu, K. Xu, Analysis of energy dissipation and crack evolution law of sandstone under impact load. International Journal of Rock Mechanics and Mining Sciences **132**, 104359 (2020). DOI: https://doi.org/10.1016/j.ijrmms.2020.104359

[18] R.X. Shen, Z.J. Gu, Z.T. Liu, E.L. Zhao, Z.S. Zang, X. Zhou, X.L. Li, W. Liu, X. Wang, Study on Impact Dynamic Behavior and Failure Characteristics of Coal based on True Triaxial Split–Hopkinson Pressure Bar Experiments. Natural Resources Research **32** (6), 2845-2866 (2023). DOI: https://doi.org/10.1007/s11053-023-10263-8

[19] P. Feng, F. Dai, Y. Liu, H.B. Du, Mechanical behaviors of rock-like specimens with two non-coplanar fissures subjected to coupled static-dynamic loads. Engineering Fracture Mechanics **199**, 692-704 (2018). DOI: https://doi.org/10.1016/j.engfracmech.2018.07.009

[20] Y.C. Wu, L.Q. Huang, X.B. Li, Dynamic compression behaviors of heat-treated granite under combined dynamic and static load. Bulletin of Engineering Geology and the Environment **83** (5), 199 (2024). DOI: https://doi.org/10.1007/s10064-024-03664-3

[21] H. Rouhani, E. Farrokh, Failure analysis of Nehbandan granite under various stress states and strain rates using a calibrated Riedel-Hiermaier-Thoma constitutive model. Geomechanics and Geophysics for Geo-energy and Geo-resources **10** (1), 157 (2024). DOI: https://doi.org/10.1007/s40948-024-00876-5

[22] X.B. Li, Y. Zou, Z.L. Zhou, Numerical Simulation of the Rock SHPB Test with a Special Shape Striker Based on the Discrete Element Method. Rock Mechanics and Rock Engineering **47** (5), 1693-1709 (2014). DOI: https://doi.org/10.1007/s00603-013-0484-6

[23] K.Q. Liu, H.Y. Liu, F.J. Zhu, X.H. Zheng, Numerical study on dynamic mechanical properties of multi-jointed rock mass under impact loading using continuous-discrete coupling model. Environmental Earth Sciences **83** (10), 309 (2024). DOI: https://doi.org/10.1007/s12665-024-11632-z

[24] Z.Y. Han, K. Liu, J.Y. Ma, D.Y. Li, Numerical simulation on the dynamic mechanical response and fracture mechanism of rocks containing a single hole. International Journal of Coal Science & Technology **11** (1), 64 (2024). DOI: https://doi.org/10.1007/s40789-024-00718-5

[25] T.T. Liu, W.X. Huang, C. Xiang, Q. Dong, X.P. Li, C. Zhang, Three-dimensional numerical simulation of dynamic strength and failure mode of a rock mass with cross joints. International Journal of Coal Science & Technology **11** (1), 17 (2024). DOI: https://doi.org/10.1007/s40789-024-00665-1

[26] D. Fukuda, M. Mohammadnejad, H.Y. Liu, Q.B. Zhang, J. Zhao, S. Dehkhoda, A. Chan, J. Kodama, Y. Fujii, Development of a 3D hybrid finite-discrete element simulator based on GPGPU-Parallelized computation for modelling rock fracturing under quasi-static and dynamic loading conditions. Rock Mechanics and Rock Engineering **53** (3), 1079-1112 (2020). DOI: https://doi.org/10.1007/s00603-019-01960-z

[27] X.S. Li, W.X. Gao, L.J. Guo, Z. Li, S.H. Zhang, Influences of the number of non-consecutive joints on the dynamic mechanical properties and failure characteristics of a rock-like material. Engineering Failure Analysis **146**, 107101 (2023). DOI: https://doi.org/10.1016/j.engfailanal.2023.107101

[28] P. Hesammokri, B. Lukic, P. Isaksson, High-strain-rate fracture behavior of rock-like materials: Insights from Split Hopkinson Pressure Bar testing and dynamic phase-field modeling. Theoretical and Applied Fracture Mechanics **141**, 105295 (2026). DOI: https://doi.org/10.1016/j.tafmec.2025.105295

[29] C.J. Li, Y. Xu, Y.T. Zhang, H.L. Li, Study on energy evolution and fractal characteristics of cracked coal-rock-like combined body under impact loading. Chinese Journal of Rock Mechanics and Engineering **38** (11), 2231-2241 (2019). DOI: https://doi.org/10.13722/j.cnki.jrme.2019.0446

[30] R. Zhao, M. Tao, C.Q. Wu, X.B. Li, S.F. Wang, Study on size and load rate effect of dynamic fragmentation and mechanical properties of marble sphere. Engineering Failure Analysis **142**, 106814 (2022). DOI: https://doi.org/10.1016/j.engfailanal.2022.106814

[31] Q.Q. Su, J.L. Cai, Dynamic mechanical behavior of sandstone with filled joints at varying angles under coupled triaxial static and dynamic loading. Structures **62**, 106169 (2024). DOI: https://doi.org/10.1016/j.istruc.2024.106169

[32] J.F. Jin, Y. Wang, L.X. Fang, H.Y. Xiong, Y.F. Xiao, X.W. Peng, Water pressure and axial static stress are influential factors on the evolution of impact energy and damage characteristics of red sandstones. Journal of China Coal Society **49** (11), 4441-4455 (2024). DOI: https://doi.org/10.13225/j.cnki.jccs.2023.1319

[33] Y.R. Li, R.Q. Huang, Relationship between joint roughness coefficient and fractal dimension of rock fracture surfaces. International Journal of Rock Mechanics and Mining Sciences **75**, 15-22 (2015). DOI: https://doi.org/10.1016/j.ijrmms.2015.01.007

[34] H. Sun, X.L. Liu, J.B. Zhu, Correlational fractal characterisation of stress and acoustic emission during coal and rock failure under multilevel dynamic loading. International Journal of Rock Mechanics and Mining Sciences **117**, 1-10 (2019). DOI: https://doi.org/10.1016/j.ijrmms.2019.03.002

[35] G.H. Erharter, Rock Mass Structure Characterization Considering Finite and Folded Discontinuities: A Parametric Study. Rock Mechanics and Rock Engineering **57** (7), 5229-5249 (2024). DOI: https://doi.org/10.1007/s00603-024-03787-9

[36] C.J. Li, Y. Xu, P.Y. Chen, H.L. Li, P.J. Lou, Dynamic Mechanical Properties and Fragment Fractal Characteristics of Fractured Coal-Rock-Like Combined Bodies in Split Hopkinson Pressure Bar Tests. Natural Resources Research **29** (5), 3179-3195 (2020). DOI: https://doi.org/10.1007/s11053-020-09656-w

[37] R.D. Peng, Y. Ju, J.G. Wang, H.P. Xie, F. Gao, L.T. Mao, Energy Dissipation and Release During Coal Failure Under Conventional Triaxial Compression. Rock Mechanics and Rock Engineering **48** (2), 509-526 (2015). DOI: https://doi.org/10.1007/s00603-014-0602-0

[38] X.P. Zhou, L.Y. Han, J. Bi, Y.D. Shou, Experimental and numerical study on dynamic mechanical behaviors of shale under true triaxial compression at high strain rate. International Journal of Mining Science and Technology **34** (2), 149-165 (2024). DOI: https://doi.org/10.1016/j.ijmst.2023.12.006

[39] Z.L. Zhou, Y. Zhao, Y.H. Jiang, Y. Zou, X. Cai, D.Y. Li, Dynamic behavior of rock during its post failure stage in SHPB tests. Transactions of Nonferrous Metals Society of China **27** (1), 184-196 (2017). DOI: https://doi.org/10.1016/S1003-6326(17)60021-9

[40] S.K. Zhao, S.Y. Wei, L. Zhang, X.G. Tian, X.Z. Yang, X. Wang, Dynamic mechanical response and crack evolution law of raw coal loaded by dynamic-static coupling under three-dimensional constraints. Scientific Reports **14** (1), 8659 (2024). DOI: https://doi.org/10.1038/s41598-024-59135-y

[41] A.L. Lu, D.Z. Song, Z.L. Li, X.Q. He, L.M. Dou, Y.R. Xue, H.K. Yang, Numerical Simulation Study on Pressure-Relief Effect of Protective Layer Mining in Coal Seams Prone to Rockburst Hazard. Rock Mechanics and Rock Engineering **57** (8), 6421-6440 (2024). DOI: https://doi.org/10.1007/s00603-024-03826-5